Orbital-free density functional theory study of crystalline Li–Si alloys

Junchao Xia [a], Emily A. Carter [a,b,*]

[a] Department of Mechanical and Aerospace Engineering, Princeton University, Princeton, NJ 08544-5263, United States
[b] Program in Applied and Computational Mathematics, and Andlinger Center for Energy and the Environment, Princeton University, Princeton, NJ 08544-5263, United States

HIGHLIGHTS

- Orbital-free density functional theory (OFDFT) is used to study Li–Si alloys.
- Accurate cell lattice vectors, bulk moduli, and densities are predicted by OFDFT.
- OFDFT elastic constants and alloy formation energies agree well with KSDFT.
- OFDFT Li atom adsorption energies on a Si(100) surface are close to KSDFT values.
- Linear-scaling OFDFT appears quite promising for large-scale Li–Si simulations.

ARTICLE INFO

ABSTRACT

Li–Si interactions are of great interest currently due to the potential use of silicon anodes in Li-ion batteries. As a first step toward eventual nanoscale characterization of lithiation of silicon, here we study the crystalline Li–Si alloys LiSi, $Li_{12}Si_7$, Li_7Si_3, $Li_{13}Si_4$, $Li_{15}Si_4$, and $Li_{22}Si_5$ using orbital-free density functional theory (OFDFT). The recently proposed Wang–Govind–Carter decomposition (WGCD) and Huang–Carter (HC) kinetic energy density functionals (KEDFs) are used to evaluate the electron kinetic energy. Both KEDFs predict accurate cell lattice vectors, equilibrium volumes, bulk moduli, and ground-state densities when compared to Kohn–Sham density functional theory (KSDFT) benchmarks. Elastic constants and alloy formation energies calculated with the WGCD KEDF also agree reasonably well with KSDFT. Finally, Li atom adsorption energies on the Si(100) − 2 × 1 surface are calculated as a simple initial test of the Li–Si mixing process during lithiation of silicon. The OFDFT adsorption energies again are fairly close to KSDFT values. The results in this work demonstrate the accuracy of the WGCD and HC KEDFs for materials with mixed covalent-metallic character and their considerable transferability under different chemical environments. Because of its quasilinear scaling, coupled with the level of accuracy shown here, OFDFT appears quite promising for large-scale simulation of such materials phenomena.

© 2013 Elsevier B.V. All rights reserved.

1. Introduction

Lithium ion batteries (LIBs) feature many attractive advantages including high energy density, light weight, and few environmental concerns, which have led to LIBs dominating the rechargeable battery market in portable electronics in recent decades. At present, most commercial LIBs use graphite-based materials as the anode. They are outstanding in terms of low cost, good durability, non-toxicity, and reasonable energy density. However, to extend the use of LIBs in, e.g., storage for stationary power applications requires further improvement of the energy density, which has encouraged intensive research efforts in recent years. Si-based materials have been recognized as a promising candidate for the anode material [1–4] due to silicon's extraordinarily high charge capacity, 3572 mAh g^{-1}, compared to 372 mAh g^{-1} for graphite [5–7]. However, during the lithiation process, the Si-based material undergoes significant structural change and volume expansion up to 300% [8–10]. Various crystalline phases including $Li_{12}Si_7$, Li_7Si_3, $Li_{13}Si_4$, $Li_{15}Si_4$, and $Li_{22}Si_5$ have been observed experimentally during high temperature lithiation [11–17]. At room temperature, lithiation also frequently induces a crystalline-to-amorphous transformation in the material [1–3]. At full lithiation of silicon, the crystalline $Li_{15}Si_4$ phase forms [2,3]. The complex structural changes along with the massive volume expansion lead to large

* Corresponding author. Department of Mechanical and Aerospace Engineering, Princeton University, Princeton, NJ 08544-5263, United States. Tel.: +1 609 258 5391; fax: +1 609 258 5877.
E-mail address: eac@princeton.edu (E.A. Carter).

stresses in the material, which cause particle fracture, capacity loss, and thus limited charge/discharge cycling capability. It is therefore critical to understand the intrinsic mechanical properties and mixing mechanisms during lithiation and delithiation in Li–Si alloys. Armed with such insight, it may be possible to render Si-based materials practical for LIB anode applications.

A number of investigations have been carried out on Li–Si materials in recent years [18–28]. In particular, first-principles computations using Kohn–Sham (KS) density functional theory (DFT) have provided many valuable predictions of mechanical properties and electronic structures for both crystalline and amorphous Li–Si alloys [18–21]. Some KSDFT studies [22–28] also investigated the dynamics of Li in Si anodes and mixing mechanisms during lithiation or delithiation. However, KSDFT's expensive (typically cubic scaling) computational cost limits current simulations to ~200 atoms. It thus prevents probing many interesting features and phenomena, which require large-scale simulation (thousands of atoms), such as fracture at surfaces or crystalline/amorphous interfaces in nanoparticles [29–31].

Orbital-free (OF) DFT [32], an alternative within the DFT formalism, uses the electron density as the sole variable and computes energies using only density functionals. By avoiding k-point sampling and orbital orthogonalization procedures necessary in KSDFT, OFDFT scales quasi-linearly with system size with a small prefactor. Calculations with thousands of atoms are now routine in OFDFT simulations, and a benchmark simulation of more than a million atoms was carried out more than four years ago with reasonable computer resources (<200 processors) [33]. A number of OFDFT studies have been reported in recent years, showing instructive and promising results for many practical materials and properties [33–44].

However, OFDFT's enormous simplification in formalism also limits its accuracy and generality. Approximating the exact non-interacting kinetic energy via kinetic energy density functionals (KEDFs) is the major challenge in OFDFT. Modern nonlocal KEDFs such as the Chacon–Alvarellos–Tarazona (CAT) [45–48], Wang–Teter (WT) [49–52], and Wang–Govind–Carter (WGC) [53] KEDFs all rely on the Lindhard linear response theory [54–56] and therefore are expected to be accurate only for nearly-free-electron-like systems such as main group metals (since the Lindhard response function is the response function of a perturbed uniform electron gas). Consequently, the OFDFT applications mentioned earlier are mostly confined to main group metals and their alloys. For other systems, such as semiconductors, transition metals, or molecules, OFDFT has been far less reliable due, until recently (*vide infra*), to the lack of KEDFs suitable for describing them.

The electronic structures of Li–Si alloys are complicated. Experimentally, many of these alloys such as $Li_{12}Si_7$ [57], Li_7Si_3 [58], and $Li_{15}Si_4$ [59] have been observed to be semiconductors with small band gaps. Nevertheless, recent KSDFT studies [20,21] predicted all these alloys to be metallic, which is not surprising considering the typical band gap underestimation by KSDFT. Despite their metallic nature predicted by KSDFT, the electron density distributions in these systems are still far from nearly-free-electron-like. A close examination of their atomic structures reveals Si–Si bonds remaining in some of the crystalline and also all amorphous phases [20,22,27], where electrons are comparatively localized. Consequently, these systems feature mixed metallic-covalent character and thus we would expect that the KEDFs mentioned above will not be able to describe them properly; indeed this will be shown in the present work.

Only very recently have several models been proposed aiming to design advanced KEDFs for covalent materials [60,61]. Specifically,

the Huang–Carter (HC) KEDF [60] focuses on linear response properties in semiconductors, and the Wang–Govind–Carter-decomposition (WGCD) [61] model decomposes the total density into localized and delocalized parts to treat them separately with different KEDFs. They both exhibited remarkable accuracy for various semiconductors [60,61] and molecules [61,62]. However, the materials examined in these studies such as cubic diamond (CD) Si, cubic zinc blende (ZB) and hexagonal wurtzite III–V semiconductors were still relatively simple structures. Furthermore, both KEDFs contain parameters that may need adjustment depending on the type of materials under investigation. Therefore, their transferability beyond reported simple semiconductors still requires further verification for more complex materials. In this work, we use the HC and WGCD KEDFs to study the crystalline Li–Si alloys including LiSi, $Li_{12}Si_7$, Li_7Si_3, $Li_{13}Si_4$, $Li_{15}Si_4$, and $Li_{22}Si_5$. We employ universal parameters in both KEDFs for a wide range of Li concentrations in these alloys, aiming to test their transferability under different chemical environments. OFDFT using either KEDF reproduces reasonably well a variety of KSDFT benchmark properties, including cell lattice vectors, equilibrium volumes, bulk moduli, elastic constants, ground-state densities, and surface adsorption energies. The results of this work validate the physics contained in both KEDF models, and also promise a bright future for OFDFT in modeling practical materials and properties beyond simple metals and alloys.

In the following, we first briefly introduce the OFDFT formalism and KEDF models in Section 2. Numerical details are described thereafter in Section 3. In Section 4, we first discuss the use of local electron-ion pseudopotentials, and then compare OFDFT and KSDFT predictions of various properties for different alloys. Finally, conclusions and outlook are given in Section 5.

2. Formalism

The Hohenberg–Kohn theorems [63] prove that the electronic total energy can be expressed as a functional of the total electron density. Specifically, it can be decomposed in the following way [64] (all formulas use atomic units):

$$E[\rho_{total}] = T_s[\rho_{total}] + J[\rho_{total}] + E_{xc}[\rho_{total}] + \int V_{ext}(\mathbf{r})\rho_{total}(\mathbf{r})d\mathbf{r},$$

(1)

where T_s is the non-interacting electron kinetic energy, J is the Hartree electron–electron repulsion energy, E_{xc} is the electron exchange-correlation (XC) energy which accounts for all errors caused by approximating the exact interacting kinetic energy and electron–electron interaction energy with T_s and J, V_{ext} is the external potential such as ionic potentials, and ρ_{total} is the total electron density. The Hartree and XC terms are trivial to compute as long as only density-dependent XC functionals such as local density approximations or generalized gradient approximations (GGAs) are used. However, the ionic potentials and T_s terms also need to be approximated in OFDFT. Evaluating the kinetic energy with the Laplacian operator is impossible without orbitals and the commonly-used, more accurate, flexible nonlocal pseudopotentials (NLPSs) cannot be used in OFDFT, also because of the lack of orbitals. Many local pseudopotentials have been proposed. In this work, we use bulk-derived local pseudopotentials (BLPSs) [62,65–67].

The major source of error in OFDFT lies in the approximation of T_s via KEDFs. In this work, we apply the WT, WGC, CAT (Sec. IV A in Ref. [48]), HC, and WGCD KEDFs to Li–Si alloys. In modern KEDF theories, nonlocal forms are usually adopted and the T_s term generally can be written as [52]:

$$T_s[\rho_{\text{total}}] = T_{\text{TF}}[\rho_{\text{total}}] + T_{\text{vW}}[\rho_{\text{total}}] + T_{\text{NL}}[\rho_{\text{total}}], \quad (2)$$

where $T_{\text{TF}}[\rho_{\text{total}}] = 3/10(3\pi)^{2/3} \int \rho_{\text{total}}^{5/3} \mathbf{dr}$ [68–70], $T_{\text{vW}}[\rho_{\text{total}}] = 1/8 \int |\nabla \rho_{\text{total}}|^2 / \rho_{\text{total}} \mathbf{dr}$ (vW) [71], and

$$T_{\text{NL}}[\rho_{\text{total}}] = C \int \int \rho_{\text{total}}^{\alpha}(\mathbf{r}) \omega(\xi(\mathbf{r},\mathbf{r}'), |\mathbf{r}-\mathbf{r}'|) \rho_{\text{total}}^{\beta}(\mathbf{r}') \mathbf{dr}\mathbf{dr}', \quad (3)$$

where C, α, and β are model-dependent constants. The nonlocal term of the CAT KEDF [48] is a bit different, but fundamentally similar in physics. The kernel ω is determined by enforcing the response function to be the Lindhard response function when a uniform electron density is reached. In Equation (3), the Fermi wave vector $\xi(\mathbf{r},\mathbf{r}')$ can either be a constant as in the WT functional, or density-dependent as in the CAT and WGC functionals.

The HC KEDF also adopts the nonlocal form shown above, but additionally considers a gradient term to approximately account for $1/|\mathbf{r}-\mathbf{r}'|$ behavior in the response function in semiconductors (see Ref. [60] for the detailed formalism). Specifically,

$$\xi(\mathbf{r},\mathbf{r}') = [3\pi\rho_{\text{total}}(\mathbf{r})]^{1/3} \left(1 + \lambda \frac{|\nabla \rho_{\text{total}}(\mathbf{r})|^2}{\rho_{\text{total}}(\mathbf{r})^{4/3}} \right). \quad (4)$$

There are two parameters in the model. λ is the parameter containing the key physics: a nonzero λ takes the gradient term or $1/|\mathbf{r}-\mathbf{r}'|$ into account and therefore is optimal for semiconductors; for metallic phases, λ should be set to smaller values or zero, which leads to a single-density-dependent form of the WGC KEDF. β is the other adjustable parameter ($\alpha + \beta = 8/3$), however it has less influence on most properties [60].

The WGCD model [61] focuses on decomposition of the total density into a localized density component such as in covalent bond regions, and a delocalized density such as in interstitial regions of all materials or everywhere in simple (non-transition) metals:

$$\rho_{\text{total}}(\mathbf{r}) = \rho_{\text{loc}}(\mathbf{r}) + \rho_{\text{del}}(\mathbf{r}), \quad (5)$$

where ρ_{loc} and ρ_{del} are the localized and delocalized densities, respectively. Different KEDF models are chosen to separately describe localized densities, delocalized densities, and their interaction energy. By using the same semi-local KEDFs for the localized density and interaction terms, and the WGC KEDF for the delocalized density, the total non-interacting kinetic energy can be approximated as:

$$T_s[\rho_{\text{total}}] = \left(T_s^{\text{semilocal}}[\rho_{\text{total}}] - T_s^{\text{semilocal}}[\rho_{\text{del}}] \right) + T_s^{\text{WGC}}[\rho_{\text{del}}], \quad (6)$$

and

$$T_s^{\text{semilocal}}[\rho] = aT_{\text{TF}}[\rho] + bT_{\text{vW}}[\rho], \quad (7)$$

as used in previous work [61]. Another key idea in the WGCD model is to only make use of density information to identify where electrons are localized and in turn to use that information to decompose the density. The WGCD scale function to calculate the delocalized density has the form:

$$F(\mathbf{r}) = f\left(\rho_{\text{total}}(\mathbf{r})/\rho_0^{\text{del}} - m \right), \quad (8)$$

and

$$\rho_{\text{del}}(\mathbf{r}) = \rho_{\text{total}}(\mathbf{r}) \times F(\mathbf{r}), \quad (9)$$

where ρ_0^{del} is the average of the delocalized density and m is a shift parameter. The form of f is numerically constructed as in Ref. [61].

There are three parameters in the WGCD KEDF besides the original parameters in the WGC functional. The shift parameter m in the scale function is the critical parameter, which determines the level of density scaling in different systems. m equal to zero is optimal and transferable for various semiconductors; larger m values gradually revert the WGCD model back to the WGC KEDF, and therefore are optimal for metallic phases. The other two parameters, a and b, in the semi-local KEDF have smaller effects on most properties though absolute energies can change slightly [61].

3. Numerical details

All OFDFT calculations are performed with our PROFESS 2.0 code [72]. Previously reported Li [67] and Si [62] BLPSs constructed with the Perdew–Burke–Ernzerhof (PBE) [73] GGA XC functional are used in OFDFT calculations. We compare our OFDFT–BLPS results to KSDFT with both BLPSs and the Projector Augmented Wave (PAW) method [74], where the latter utilizes nonlocal electron-ion potentials similar to NLPSs. We perform KSDFT–PAW calculations with the Vienna Ab Initio Simulation (VASP) Package [75–77], and KSDFT-BLPS calculations with the ABINIT code [78]. The PBE [73] form of GGA is used as the XC functional in all calculations in this work.

In all calculations, kinetic energy cutoffs for the plane wave basis are chosen to converge total energies to within 1 meV per atom for each system. We use 1600 eV for all OFDFT calculations (equivalent to 400 eV in ABINIT in terms of grid size). Detailed kinetic energy cutoffs and k-point sampling information for KSDFT calculations are listed in Table 1 for all structures studied in this work, along with their symmetry space groups and numbers of atoms in unit cells. Fermi–Dirac smearing with a smearing width equal to 0.1 eV is used for all structures except for bulk CD Si and Si(100) − 2 × 1 surface adsorption where no smearing is used.

We test the WT, CAT, WGC, HC, and WGCD KEDFs in OFDFT calculations. For the WT KEDF, $\alpha = \beta = 5/6$. We use the specific form of the CAT functional following the equations (12), (23), and (24) in Ref. [48], where we set $\alpha = 3/5$, $\beta = 1$, and $\gamma = 1.4$. WGC calculations are very difficult to converge for these Li–Si alloy systems due to the Taylor expansion evaluation (required to retain quasilinear scaling) [53]. We have tuned large ranges of parameters of α, γ, and the density expansion center ρ^*, and find it can only converge for one of the alloys, $Li_{15}Si_4$, using the universally-derived density exponents $\alpha = (5 - \sqrt{5})/6$, $\beta = 5/3 - \alpha$, $\gamma = 3.6$, and $\rho^* = \rho_0$ [52,53]. For the HC

Table 1
Space groups and numbers of Li and Si atoms in unit cells for all systems studied in this work. The kinetic energy cutoffs (in eV) used in ABINIT KSDFT–BLPS and VASP KSDFT–PAW calculations and numbers of irreducible k-points in all KSDFT calculations are also listed.

Systems	Space group	#Li/Si	ABINIT E_{cutoff}	VASP E_{cutoff}	k-Points
Si	Fd-3m (227)	0/2	900	400	256
LiSi	I41/a (88)	8/8	900	300	126
Li$_{12}$Si$_7$	Pnma (62)	96/56	600	300	27
Li$_7$Si$_3$	P3$_2$12 (153)	42/18	900	300	34
Li$_{13}$Si$_4$	Pbam (55)	26/8	900	300	125
Li$_{15}$Si$_4$	I-43d (220)	30/8	900	300	10
Li$_{22}$Si$_5$	F23 (196)	88/20	600	300	4
Li	Im-3m (229)	2/0	900	300	250
Li on Si surface	–	2/24	900	400	28

KEDF, we adjust λ and β values to obtain reasonable bulk properties and energetics. We find intermediate values of $\lambda = 0.006$ and $\beta = 0.65$ produce optimal results for equilibrium volumes and bulk moduli of all alloys compared to KSDFT benchmarks. This parameter set is used to calculate all phases to examine its transferability. In WGCD calculations, we keep $m = 0$, which is optimal for CD Si, as reported previously [61]. We only adjust a and b values in the semi-local KEDF. First, $a = 0.835$ and $b = 0.679$ (universal averaged values from various semiconductors found in previous work) [61] are tested to see their transferability in these more complicated Li–Si alloy phases. We then slightly re-adjust these two parameters and find $a = 0.810$ and $b = 0.6$ generate slightly better alloy formation energies (by ~ 0.1 eV) and similar bulk properties. These two parameter sets are both applied to calculate all phases. Further fine tuning can lead to optimal parameters for each phase, respectively, giving even better bulk properties (by $\sim 1\%$ for equilibrium volumes and ~ 5 GPa for bulk moduli); the optimal parameters for each alloy are not identical but all very close to those above. Since the universal parameter sets also predict reasonable results and using the same Hamiltonian for different systems allows us to make rigorous comparisons, we do not report the results calculated with different optimal parameters. Finally, the parameters in the WGC KEDF when performing WGCD calculations are the same as reported previously [61]. When using the WGCD model to do Si surface calculations, particular care needs to be taken when calculating average densities. See details in Sec. III of Ref. [61].

For each alloy, we compute equilibrium volumes, bulk moduli, and alloy formation energies. All structures are first fully relaxed in KSDFT calculations. An atomic force tolerance of 2×10^{-4} hartree–bohr^{-1} (1 hartree = 27.2114 eV, 1 bohr = 0.529 Å) is used in VASP and 5×10^{-5} hartree-bohr^{-1} in ABINIT. The default stress tensor thresholds in both VASP and ABINIT are used. In OFDFT calculations, we fix atomic internal coordinates from KSDFT–BLPS calculations and optimize cells by manually scanning degrees of freedom in lattice vectors (stress tensors for the WGCD KEDF are not available yet in PROFESS; atomic forces are available but OFDFT ion relaxation for these complicated alloy structures is still not accurate enough and needs further investigation that is left for future work). After obtaining equilibrium lattice vectors, we expand and compress the cell isotropically by up to 2% with atomic internal coordinates fixed. For HC KEDF calculations only, a $\pm 5\%$ volume change is adopted due to numerical convergence difficulties during interpolation (a large number of interpolation bins is needed for convergence to 1 meV per atom; a small number of bins leads to noisy curves on a fine energy scale). The energy versus volume curves are then fit to Murnaghan's equation of state [79] to compute bulk moduli. The alloy formation energies are calculated according to the equation:

$$E_f = E_{Li_xSi_{1-x}} - xE_{Li} - (1-x)E_{Si}, \qquad (10)$$

where $E_{Li_xSi_{1-x}}$ is the total energy per atom and x is the atomic concentration of Li in each alloy. E_{Li} is the total energy per Li in the body-centered-cubic (bcc) phase and E_{Si} is the total energy per Si in the CD phase, which are the ground-state phases of each element under ambient conditions.

We calculate C_{11}, C_{22}, C_{33}, C_{44}, C_{55}, C_{66}, C_{23}, C_{13}, C_{12} for all phases, and additionally C_{26} for LiSi. In each elastic constant calculation, we apply a strain tensor, ε, to the equilibrium structure:

$$\begin{pmatrix} a'_1 \\ a'_2 \\ a'_3 \end{pmatrix} = \begin{pmatrix} a_1 \\ a_2 \\ a_3 \end{pmatrix} \cdot (1 + \varepsilon), \qquad (11)$$
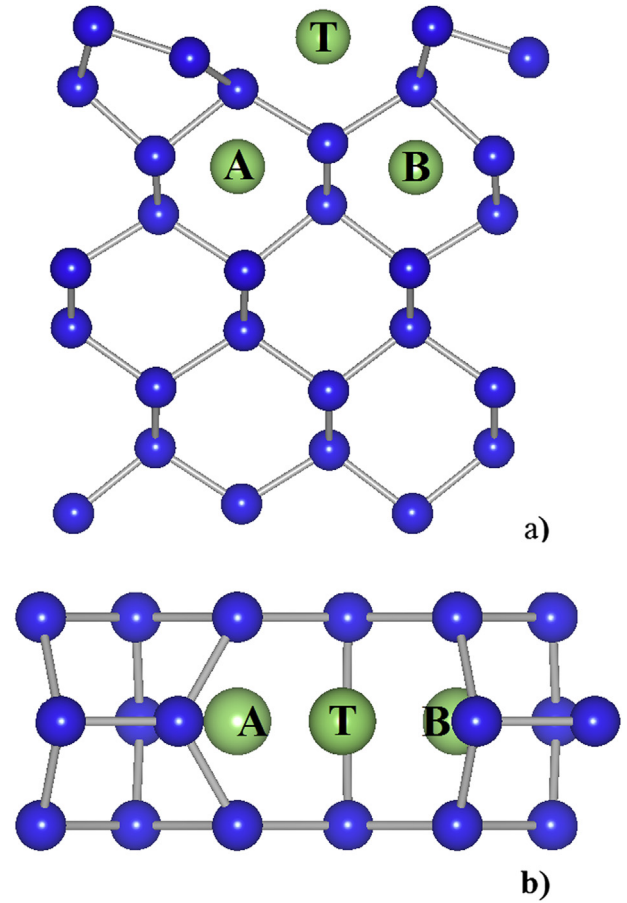
where a_i are primitive lattice vectors and

Fig. 1. a) Side view and b) top view of the reconstructed Si(100) surface with a $p(2 \times 1)$ geometry. Three different sites T, A, and B are selected for Li atom adsorption calculations. The figure was produced with the VESTA software [80].

$$\varepsilon = \begin{pmatrix} e_{xx} & e_{xy} & e_{zx} \\ e_{xy} & e_{yy} & e_{yz} \\ e_{zx} & e_{yz} & e_{zz} \end{pmatrix}, \qquad (12)$$

where e_{ij} are strain components defined in Cartesian coordinates. The strain energy resulting from the deformation can be expressed:

$$E = E_0 + \frac{V_0}{2} \mathbf{e}\mathbf{C}\mathbf{e}^T, \qquad (13)$$

where E_0 and V_0 are the total energy and volume of the equilibrium structure, $e = (e_{xx}, e_{yy}, e_{zz}, 2e_{yz}, 2e_{xz}, 2e_{xy})$, and $\mathbf{C}$ is the stiffness tensor. For C_{11}, C_{22}, and C_{33}, e is set to be $(\delta, 0,0,0,0,0)$, $(0,\delta,0,0,0,0)$, and $(0,0,\delta,0,0,0)$, respectively, where deformation range δ is within $\pm 1\%$. The resulting total energy versus δ data is fit to the quadratic function

$$E = E_0 + \frac{1}{2} C\delta^2 V_0, \qquad (14)$$

to calculate the corresponding elastic constant. Similarly, for C_{44}, C_{55}, and C_{66}, e is set as $(0,0,0,2\delta,0,0)$, $(0,0,0,0,2\delta,0)$, and $(0,0,0,0,0,2\delta)$, respectively and fit to

$$E = E_0 + 2C\delta^2 V_0. \qquad (15)$$

To calculate C_{12}, $e = (\delta,\delta,0,0,0,0)$ and then we fit to

$$E = E_0 + \frac{1}{2}(C_{11} + C_{22} + 2C_{12})\delta^2 V_0. \tag{16}$$

Similarly $e = (\delta,0,\delta,0,0,0)$ and $e = (0,\delta,\delta,0,0,0)$, and

$$E = E_0 + \frac{1}{2}(C_{11} + C_{33} + 2C_{13})\delta^2 V_0, \tag{17}$$

$$E = E_0 + \frac{1}{2}(C_{22} + C_{33} + 2C_{23})\delta^2 V_0, \tag{18}$$

are used for C_{13} and C_{23} calculations, respectively. To calculate C_{26}, $e = (0,\delta,0,0,0,2\delta)$ and the equation

$$E = E_0 + \frac{1}{2}(C_{22} + 4C_{66} + 4C_{26})\delta^2 V_0, \tag{19}$$

are used to do the fitting. Due to the convergence difficulties with the HC KEDF, we only employ the WGCD KEDF in OFDFT to calculate elastic constants.

Finally, Li atom adsorption on the reconstructed $\text{Si}(100) - 2 \times 1$ surface is studied. We report results of spin-unpolarized calculations; we also did spin-polarized calculations and found almost no differences ($<10^{-3}$ meV per atom). We use a $p(2 \times 1)$ geometry with 12 layers (24 atoms) for the $\text{Si}(100) - 2 \times 1$ surface. Two Li atoms are then put in selected sites above or beneath the surfaces (Fig. 1) on both sides of the slab to avoid creating a net dipole within our periodic boundary condition calculation. 10 Å of vacuum between periodic slabs is used as a buffer so as to minimize spurious interactions between periodic images. Geometries are fully relaxed in all KSDFT calculations, while OFDFT employs KSDFT−BLPS relaxed geometries and only optimizes the electron density. The adsorption energies are calculated as

$$E_{ad} = \left(E_{surface+Li} - E_{surface} - 2E_{Li}\right)\bigg/2, \tag{20}$$

where $E_{surface+Li}$ is the total energy of the Si surface with two adsorbed Li atoms, $E_{surface}$ is the total energy of the pure Si surface, and E_{Li} is the total energy for a single Li atom. In the OFDFT calculation for single Li atom, the vW KEDF is used as it is exact for single-orbital systems (here only the 2s electron of Li is treated while the 1s electrons are subsumed into the pseudopotential).

4. Results and discussion

4.1. Validation of bulk-derived local pseudopotentials

Only local pseudopotentials (LPSs) can be used in OFDFT due to the lack of orbitals (recall that NLPSs contain orbital-based projection operators). LPSs apply an identical potential to all electrons, in contrast to NLPSs or the PAW method that apply different potentials to electrons of different angular momenta. In this work, we use previously reported BLPSs [62,67], without including a non-linear core correction [81] for either Li or Si. To ensure that our BLPSs are sufficiently accurate, we start with a set of validation tests within KSDFT. We compare structures and properties predicted by KSDFT using BLPSs benchmarked against the KSDFT-PAW method, to identify errors due to the BLPSs alone, before moving on to OFDFT calculations which will have additional errors due to the KEDFs.

The cell lattice vector ratios, b/a and c/a, in relaxed equilibrium structures are listed in Table 2. Our PAW results are all consistent with those reported in Refs. [18,20]. The differences between KSDFT−BLPS and KSDFT−PAW ratios are generally very small, of the order of 1%, except for LiSi which exhibits a deviation of 6%. The relaxed internal coordinates (not reported here) with BLPSs are also almost the same as with PAW, with the average error being less than 0.002 in fractional coordinates. The predicted equilibrium volumes and bulk moduli for each alloy are shown in Tables 3 and 4, and Fig. 2. Again, our PAW equilibrium volumes are almost the same as found in Refs. [18,20], while the PAW−GGA results in Ref. [19] are generally larger than all others. Our PAW bulk moduli are very close to the values in Ref. [20], while the bulk moduli reported in Ref. [18] are a bit smaller for $\text{Li}_{12}\text{Si}_7$ but similar for other alloys (there is one minor technical difference between the present paper and the other previous studies: in Refs. [18,20], ion positions were relaxed for deformed structures when calculating bulk moduli, while we fixed ion positions as in the equilibrium phases. Relaxing ions will lead to slightly reduced energies for deformed structures, and consequently we expect our bulk moduli to slightly exceed those from the other studies, but by no more than 5 GPa. This is similar to the elastic constant results in Section 4.3). Overall, lattice constants and equilibrium volumes obtained by BLPSs and PAW are very close to each other (Table 3); LiSi exhibits the largest deviation ($\sim 3.5\%$), consistent with the deviation in lattice vector ratios. The trend in equilibrium volumes (increasing with Li concentration) for the alloys is captured very well (Fig. 2a). More significant differences are seen in the bulk moduli (Table 4). The KSDFT−BLPS bulk moduli for the alloys are generally somewhat larger (by ~ 10 GPa) than the KSDFT−PAW moduli, but the trend of elastic softening as the Li concentration increases is correctly captured (Fig. 2b). Finally, we calculate alloy formation energies (Fig. 3). Our PAW results are consistent with Fig. 1 in Ref. [20] and Table 2 in Ref. [18], with differences less than 0.005 eV atom^{-1}. BLPS errors compared to PAW values are mostly very small, within several tens of meV; only for LiSi again, KSDFT-BLPS calculations predict a bit larger formation energy by ~ 80 meV.

Overall, the use of BLPSs does not lead to large errors in various properties predicted within KSDFT, thereby justifying their use in what follows. Next we use BLPSs in OFDFT calculations, comparing against KSDFT−BLPS benchmarks, to isolate the errors in various KEDFs while keeping the electron-ion interaction the same in both sets of calculations.

4.2. Bulk properties

We first relax cell lattice vectors. We find it is not a trivial task in OFDFT. The optimal b/a and c/a ratios obtained using the HC, WGCD, and CAT KEDFs within OFDFT are listed in Table 2 for the alloys that contain degrees of freedom in their cell lattice vectors. We do not report WGC KEDF results because it fails to converge for these alloys. Although these alloys are all predicted to be metallic in KSDFT, the density variation is still very significant (see Section 4.5). This is caused by localized electrons existing within Si−Si bonds (for LiSi, $\text{Li}_{12}\text{Si}_7$, Li_7Si_3, and $\text{Li}_{13}\text{Si}_4$) or around Si atoms (for $\text{Li}_{15}\text{Si}_4$ and $\text{Li}_{22}\text{Si}_5$). Consequently, the WGC KEDF becomes both physically and numerically unsound, and diverges when performing the

Table 2

Optimized b/a and c/a ratios of lattice vectors in Li−Si alloys. KSDFT−PAW and KSDFT−BLPS results are both given. The OFDFT results are calculated with $\lambda = 0.006$ and $\beta = 0.65$ in the HC KEDF and $m = 0$, $a = 0.835$, and $b = 0.679$ in the WGCD KEDF. See Section 3 for other numerical details.

	LiSi c/a	Li_7Si_3 c/a	$\text{Li}_{12}\text{Si}_7$ b/a	$\text{Li}_{12}\text{Si}_7$ c/a	$\text{Li}_{13}\text{Si}_4$ b/a	$\text{Li}_{13}\text{Si}_4$ c/a
KSDFT−PAW	0.614	2.370	2.299	1.675	1.904	0.559
KDFT−BLPS	0.576	2.393	2.324	1.690	1.910	0.556
OFDFT−WGCD	0.559	2.431	2.378	1.739	1.929	0.537
OFDFT−HC	0.56	2.48	2.40	1.76	1.92	0.54
OFDFT−CAT	0.517	−	−	−	−	−

Table 3
Equilibrium volumes (V_0, Å^3) per Si atom for CD Si and each Li–Si alloy, and V_0 per Li atom for bcc Li, calculated with KSDFT–PAW, KSDFT–BLPS, and OFDFT. We employ $\lambda = 0.006$ and $\beta = 0.65$ in HC calculations; $m = 0$, $a = 0.835$, and $b = 0.679$ are used in WGCD_A results and $m = 0$, $a = 0.81$, and $b = 0.6$ in WGCD_B. See Section 3 for other numerical details. The same parameter sets were used in Table 4.

	CD Si	LiSi	Li$_{12}$Si$_7$	Li$_7$Si$_3$	Li$_{13}$Si$_4$	Li$_{15}$Si$_4$	Li$_{22}$Si$_5$	bcc Li
KSDFT−PAW	20.455	31.372	42.872	49.808	66.176	74.563	81.251	20.353
KSDFT−BLPS	20.444	30.278	43.143	49.921	66.792	75.357	83.245	20.204
HC	21.600	30.115	42.375	49.457	68.006	73.791	83.044	19.803
WGCD_A	20.340	29.084	41.240	49.720	67.503	76.244	84.071	19.401
WGCD_B	20.785	28.970	40.916	49.280	67.063	75.446	83.174	19.045
WGC	23.426	–	–	–	–	67.676	–	20.208
CAT	19.566	29.170	40.049	46.723	62.402	69.423	78.851	20.272

Table 4
Bulk modulus (B, GPa) for CD Si and each Li–Si alloy, calculated with KSDFT–PAW, KSDFT–BLPS, and OFDFT.

	CD Si	LiSi	Li$_{12}$Si$_7$	Li$_7$Si$_3$	Li$_{13}$Si$_4$	Li$_{15}$Si$_4$	Li$_{22}$Si$_5$	bcc Li
KSDFT−PAW	89	60	46	42	31	30	31	14
KSDFT−BLPS	90	69	57	51	43	40	37	16
HC	74	70	53	53	40	36	38	17
WGCD_A	97	84	62	56	41	39	38	15
WGCD_B	95	86	61	55	43	40	38	15
WGC	39	–	–	–	–	58	–	16
CAT	92	84	74	66	53	54	45	16

required Taylor series expansion evaluation. The WT and CAT KEDFs, both of which are also based on the perturbed uniform electron gas, should be inappropriate for describing Li–Si alloys for the same reason. In fact, although the WT KEDF converges for all systems, the energies are unbounded, i.e., energies always decrease as volumes increase, just as found earlier for pure Si [82]. The CAT KEDF performs better than the WT KEDF presumably because it has a density-dependent kernel. It converges for every phase (only a first order expansion is needed to evaluate the CAT KEDF, unlike the WGC KEDF which requires a second order expansion) and exhibits an energy minimum versus volume with fixed b/a and c/a ratios. However, no minimum can be found when searching for optimal ratios for any alloy except for LiSi, i.e., the total energies always decrease with increasing or decreasing b/a and c/a ratios. The CAT KEDF optimized c/a ratio of LiSi is listed in Table 2, but it is not accurate when compared to KSDFT-BLPS calculations. Therefore, because of the convergence difficulties and/or lack of clear minima, all bulk properties shown hereafter for the WGC and CAT KEDFs are calculated employing KSDFT-BLPS optimized ratios (except for LiSi for the CAT KEDF). By contrast, both the WGCD and the HC KEDFs predict quite accurate ratios for all the alloys, very close to benchmark KSDFT-BLPS and even to the KSDFT−PAW results. We only report HC ratios to the second significant digit after decimal point due to the interpolation convergence difficulties mentioned in Section 3.

We next report equilibrium volumes and bulk moduli for each phase (Tables 3 and 4, and also Fig. 2). Again, WGC results for Li$_{15}$Si$_4$ and CAT results for all alloys are not satisfactory with underestimated equilibrium volumes and overestimated bulk moduli. By contrast, the HC KEDF (that describes localized covalent bonds
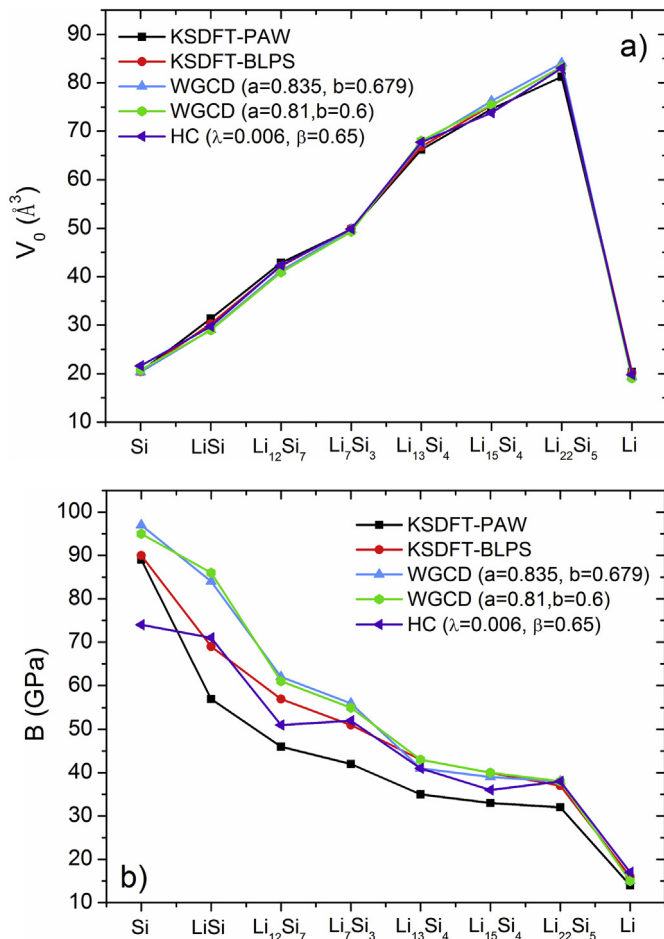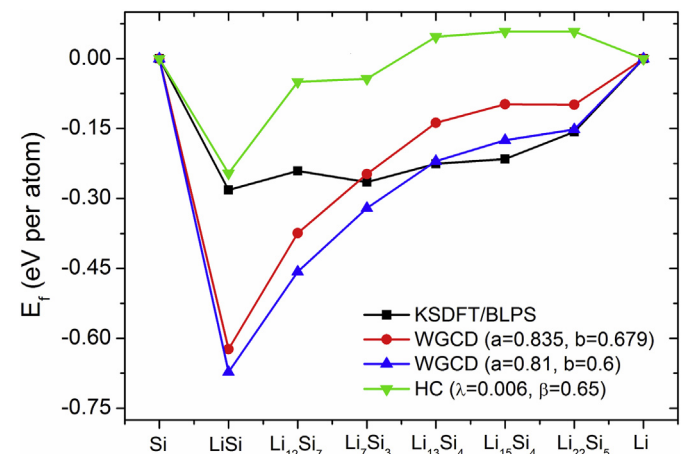

Fig. 2. a) Equilibrium volume per Si atom (Å^3) for CD Si and each Li–Si alloy, and per Li atom for bcc Li, and b) bulk modulus (GPa) for each phase, calculated with KSDFT–PAW, KSDFT–BLPS, and OFDFT. $\lambda = 0.006$ and $\beta = 0.65$ are used in OFDFT–HC calculations; for WGCD results, we report two data sets with $m = 0$, $a = 0.835$, and $b = 0.679$, as well as $m = 0$, $a = 0.81$, and $b = 0.6$.

Fig. 3. Alloy formation energies (eV) per atom (E_f) for each alloy, calculated with KSDFT−PAW, KSDFT−BLPS, and OFDFT. $\lambda = 0.006$ and $\beta = 0.65$ are used in OFDFT–HC calculations; for WGCD results, we report two data sets with $m = 0$, $a = 0.835$, and $b = 0.679$, as well as $m = 0$, $a = 0.81$, and $b = 0.6$.
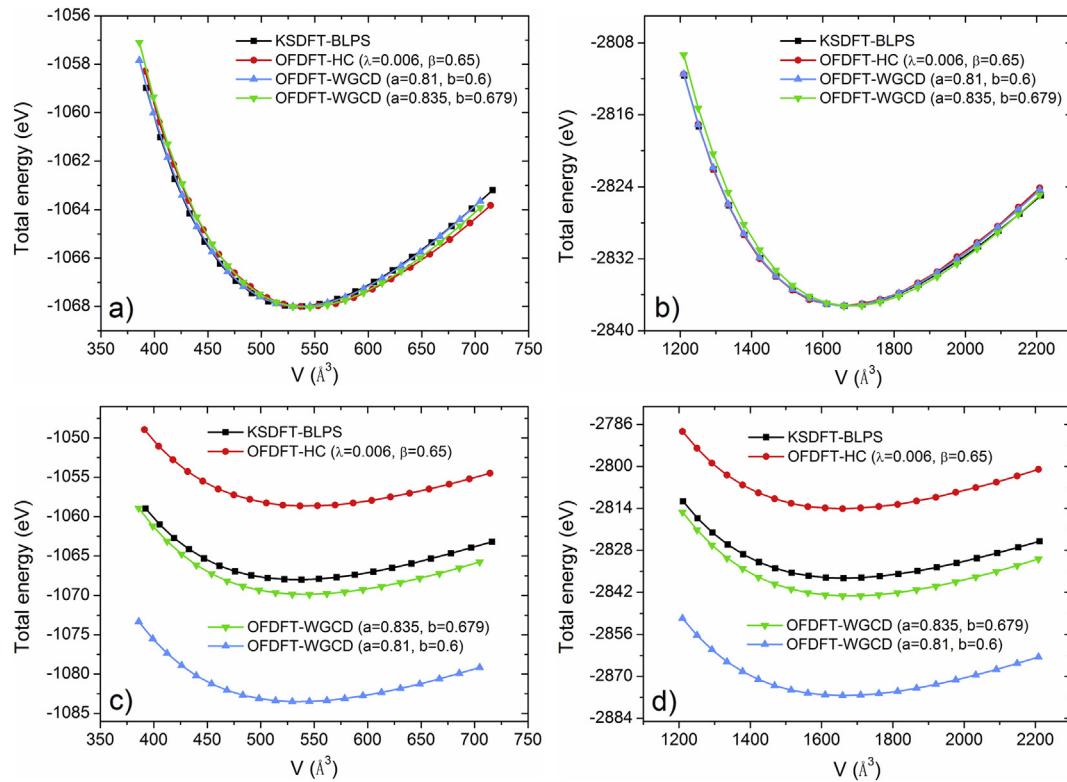
Fig. 4. Total energy versus volume per unit cell calculated with KSDFT−BLPS and OFDFT for a) Li$_{13}$Si$_4$, and b) Li$_{22}$Si$_5$ where the OFDFT curves are shifted to have the same total energy minimum as KSDFT to assist comparison, and c) Li$_{13}$Si$_4$, and d) Li$_{22}$Si$_5$ without shifting. $\lambda = 0.006$ and $\beta = 0.65$ are used in OFDFT−HC calculations; for WGCD results, we report two data sets with $m = 0$, $a = 0.835$, and $b = 0.679$, as well as $m = 0$, $a = 0.81$, and $b = 0.6$.

well) delivers equilibrium volumes and bulk moduli much closer to KSDFT−BLPS benchmarks. Likewise, the WGCD model with the universal parameter set $a = 0.835$ and $b = 0.679$ determined previously [61] demonstrates good transferability for these more complicated structures, predicting accurate equilibrium volumes and bulk moduli for all alloys; another slightly adjusted parameter set $a = 0.81$ and $b = 0.6$ also generates similar results. The absolute energies (not shown here) reveal some errors with the universal parameters but the overall trend and relative energies are still reasonable for the WGCD KEDF, as shown when calculating alloy formation energies in Section 4.4. Some energy versus volume curves are plotted as examples in Fig. 4; the shapes of OFDFT curves agree very well with KSDFT ones over a large deformation range. The WGCD KEDF with $a = 0.835$ and $b = 0.679$ generally provides the most accurate absolute total energies compared to KSDFT for all alloys (except for LiSi). Statistically, 80% of the HC and WGCD results have errors in equilibrium volumes within 3%, corresponding to less than 1% error in lattice constants. The largest error in lattice constants is also below 2%. The predicted bulk moduli are also fairly accurate compared to KSDFT-BLPS benchmarks (errors within 5 GPa), except the WGCD KEDF overestimates the LiSi bulk modulus by about 15 GPa. The general trends of volume expansion and elastic softening through the increasing Li concentration are clearly predicted by OFDFT as plotted in Fig. 2 along with KSDFT−BLPS results. Overall, we see very good agreement between OFDFT and KSDFT data.

4.3. Elastic constants

We also employ the WGCD KEDF to calculate elastic constants for every alloy as well as for bcc Li and CD Si (Table 5). Our PAW

results overall agree with Ref. [18], with some values a bit larger as discussed in Section 4.1. However, we also observe some large differences, for instance, for C_{44} of Li$_{13}$Si$_4$, C_{11}, and C_{12} of Li$_{22}$Si$_5$. We found the results reported in Ref. [83] are also very different from Ref. [18] but close to ours. Here, we focus on comparing our KSDFT and OFDFT results. The HC KEDF is not used due to its numerical

Table 5
Elastic constants (GPa) calculated with KSDFT−PAW, KSDFT−BLPS, and OFDFT−WGCD with $m = 0$, $a = 0.835$, and $b = 0.679$.

	Method	C_{11}	C_{22}	C_{33}	C_{44}	C_{55}	C_{66}	C_{12}	C_{13}	C_{23}	C_{26}
CD Si	KSDFT−PAW	160	160	160	99	99	99	55	55	55	
	KSDFT−BLPS	153	153	153	104	104	104	56	56	56	
	OFDFT−WGCD	94	94	94	44	44	44	100	100	100	
LiSi	KSDFT−PAW	105	105	85	56	56	46	18	37	37	6
	KSDFT−BLPS	130	130	102	60	60	46	22	43	43	3
	OFDFT−WGCD	157	157	148	32	32	40	51	49	49	16
Li$_{12}$Si$_7$	KSDFT−PAW	86	114	118	45	33	25	4	11	14	
	KSDFT−BLPS	113	131	134	49	40	32	12	19	22	
	OFDFT−WGCD	109	146	137	28	36	29	32	33	29	
Li$_7$Si$_3$	KSDFT−PAW	84	84	159	28	28	38	9	5	5	
	KSDFT−BLPS	114	114	171	27	27	42	30	1	1	
	OFDFT−WGCD	74	74	150	19	19	20	35	24	24	
Li$_{13}$Si$_4$	KSDFT−PAW	80	94	80	28	25	28	9	5	5	
	KSDFT−BLPS	94	98	89	32	26	38	15	11	14	
	OFDFT−WGCD	80	71	68	25	17	17	24	25	32	
Li$_{15}$Si$_4$	KSDFT−PAW	51	51	51	32	32	32	23	23	23	
	KSDFT−BLPS	63	63	63	35	35	35	29	29	29	
	OFDFT−WGCD	56	56	56	25	25	25	30	30	30	
Li$_{22}$Si$_5$	KSDFT−PAW	56	56	56	42	42	42	20	20	20	
	KSDFT−BLPS	52	52	52	42	42	42	30	30	30	
	OFDFT−WGCD	42	42	42	31	31	31	35	35	35	
bcc Li	KSDFT−PAW	14	14	14	11	11	11	14	14	14	
	KSDFT−BLPS	20	20	20	15	15	15	14	14	14	
	OFDFT−WGCD	16	16	16	16	16	16	14	14	14	

issues discussed in Section 3. For CD Si, OFDFT unfortunately predicts quite inaccurate results compared to KSDFT, consistent with our previous study [61]. As we increase the Li concentration, the results become increasingly better. This is presumably because we have more delocalized electron density in the system which can be properly described by the WGC KEDF buried in the WGCD model. For $Li_{22}Si_5$, $Li_{15}Si_4$, or $Li_{13}Si_4$, the elastic constants are in fair agreement with KSDFT−BLPS results ($Li_{15}Si_4$ deformation curves are shown in Fig. 5). The values are most accurate for bcc Li because the WGCD KEDF reverts nearly to the pure WGC KEDF, which contains the correct physics for a pure main group metal such as Li. The results are worse for other alloys such as LiSi but the magnitudes and relative ordering of elastic constants are still acceptable for most cases. On average, OFDFT produces an error of ∼ 14 GPa for all alloys compared to KSDFT−BLPS benchmarks.

4.4. Alloy formation energies

Next we calculate alloy formation energies with the HC and WGCD KEDFs. Universal parameter sets are used for all phases, with our aim to keep the same Hamiltonian for all systems and also to test the transferability of these two KEDF models. In Section 4.2, we discussed absolute energy errors in WGCD results; similar errors exist in HC results as well. In previous work [60,61], it was shown that although universal parameters lead to absolute energy errors, relative energies are quite reasonable, i.e., a common shift occurs in all total energies. However, those tests were made within very similar structures, i.e., the CD Si and ZB group III−V semiconductors. Here, we calculate very different phases ranging from the purely metallic bcc Li to purely covalent CD Si, and compare their relative energies. We regard this as the most demanding test in this work, because the parameter λ in the HC KEDF and m in the WGCD model were shown to have different optimal values when treating different materials, especially for covalent and metallic phases considered in previous work [60,61].

The resulting alloy formation energies are displayed in Fig. 3. Unfortunately, we see unphysical behavior in the HC predictions: the alloy formation energies of some alloys ($Li_{13}Si_4$, $Li_{15}Si_4$, and $Li_{22}Si_5$) are positive whereas KSDFT predicts them all to be negative. Even the three negative formation energies are also not satisfactory since they deviate significantly from the KSDFT benchmarks, except for LiSi. This illustrates the limited transferability of the HC KEDF in different chemical environments, though other bulk properties are rather reasonable. The WGCD KEDF generally performs better than the HC KEDF, at least predicting all alloys to be energetically favorable with negative formation energies, consistent with KSDFT. For Li_7Si_3, $Li_{13}Si_4$, $Li_{15}Si_4$, and $Li_{22}Si_5$, OFDFT−WGCD produces quite accurate formation energies, especially with $a = 0.81$ and $b = 0.6$. However, for $Li_{12}Si_7$ and particularly LiSi, the alloy formation
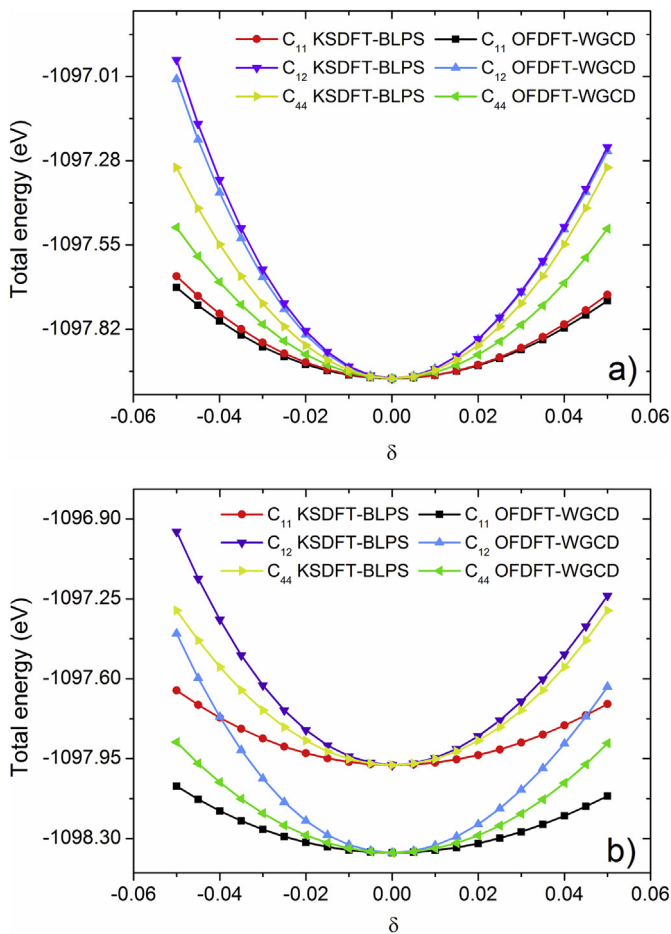

Fig. 5. Total energy per unit cell versus δ in elastic deformation of C_{11}, C_{12}, and C_{44} for $Li_{15}Si_4$, as calculated with KSDFT−BLPS and OFDFT−WGCD. a) The OFDFT curves are shifted to have the same equilibrium energy ($\delta = 0$) as KSDFT to assist comparison; b) curves without shifting. $m = 0$, $a = 0.835$, and $b = 0.679$ are used in OFDFT−WGCD calculations.
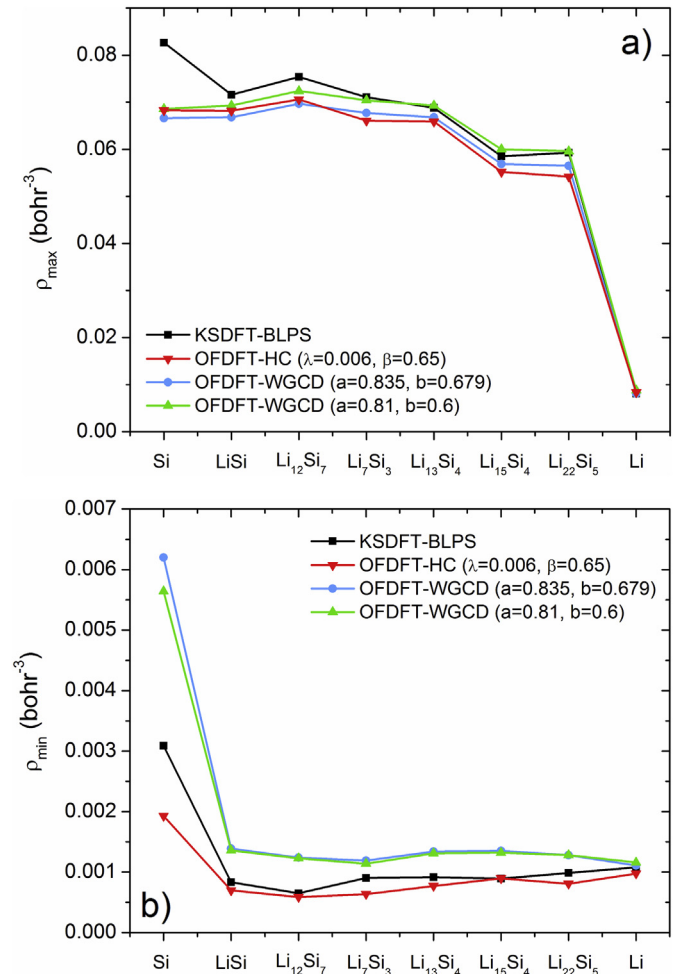

Fig. 6. a) Maximum and b) minimum densities in each phase at its equilibrium structure, calculated with KSDFT−BLPS and OFDFT. $\lambda = 0.006$ and $\beta = 0.65$ are used in OFDFT−HC calculations; for WGCD results, we report two data sets with $m = 0$, $a = 0.835$, and $b = 0.679$, as well as $m = 0$, $a = 0.81$, and $b = 0.6$.

Table 6
Li atomic concentrations x, average density ρ_0 (in 10^{-2} bohr^{-3}), and ρ_{max}/ρ_0 for each phase at its equilibrium structure calculated with KSDFT–BLPS and OFDFT–WGCD. The maximum values of the electron localization function (ELF$_{max}$) from KSDFT–BLPS calculations, ρ_{0del}/ρ_0 and ρ_{max}/ρ_{0del} from OFDFT–WGCD calculations are also listed. $m = 0$, $a = 0.835$, and $b = 0.679$ are used in WGCD calculations.

	CD Si	LiSi	Li$_{12}$Si$_7$	Li$_7$Si$_3$	Li$_{13}$Si$_4$	Li$_{15}$Si$_4$	Li$_{22}$Si$_5$	bcc Li
x	0	0.5	0.632	0.7	0.765	0.789	0.815	1
KSDFT–BLPS ρ_0	2.90	2.44	1.96	1.88	1.61	1.52	1.49	0.73
OFDFT–WGCD ρ_0	2.85	2.55	2.07	1.90	1.60	1.52	1.50	0.78
KSDFT–BLPS ρ_{max}/ρ_0	2.854	2.930	3.847	3.785	4.283	3.844	3.967	1.108
OFDFT–WGCD ρ_{max}/ρ_0	2.408	2.712	3.502	3.700	4.330	3.946	3.986	1.135
ELF$_{max}$	0.938	0.928	0.912	0.858	0.861	0.819	0.830	0.581
OFDFT/WGCD ρ_{0del}/ρ_0	0.510	0.536	0.536	0.575	0.598	0.604	0.644	0.960
OFDFT/WGCD ρ_{max}/ρ_{0del}	4.722	5.064	6.532	6.435	7.243	6.532	6.187	1.182

energies are greatly overestimated (too negative), thus giving an incorrect ordering of alloy formation stability. This demonstrates the transferability of the WGCD KEDF still requires further improvement. Overall, the WGCD model correctly favors alloy formation and thus may prove adequate for simulating lithiation of silicon, especially at high Li concentrations that are of particular practical interest.

4.5. Ground-state densities

We next compare OFDFT and KSDFT ground-state densities. The maximum and minimum densities in each alloy in their equilibrium structures are plotted in Fig. 6. The density peak in CD Si is underestimated by both HC and WGCD. Encouragingly, the underestimation is significantly smaller for the alloys. In particular, the maximum densities from WGCD with $a = 0.81$ and $b = 0.6$ are very close to those from KSDFT for most of the alloys. Other OFDFT KEDFs predict a bit smaller (by $\sim 10^{-3}$ bohr^{-3}) maximum densities. Errors in the minimum densities of the alloys are very small, on the order of 10^{-4} bohr^{-3}. Qualitatively, the WGCD model tends to overestimate the minimum density, indicating over-delocalization presumably due to the influence of the WGC KEDF within the WGCD model. By contrast, the HC KEDF predicts slightly smaller minimum densities compared to KSDFT. The general shapes of density distributions are primarily determined by positions of the nuclei and therefore are very similar in OFDFT and KSDFT calculations. Overall, though, OFDFT's maximum and minimum densities for the alloys agree quite closely with KSDFT densities.

We can also infer other physical properties qualitatively through densities. First, the OFDFT–WGCD average densities (Table 6) are very close to KSDFT ones, indicating accurate equilibrium volumes. Secondly, the ρ_{0del}/ρ_0 values in WGCD calculations (Table 6) are qualitatively consistent with the fact that the system tends to be more metallic and have more delocalized electrons as the Li concentration grows. This ratio generally increases as the Li concentration increases, implying a larger portion of delocalized electron densities. In pure bcc Li, up to 96% of the electron density is

delocalized. This trend demonstrates the rationale behind the WGCD KEDF is physically reasonable and justified. Thirdly, we see quite large maximum electron localization function (ELF) [84,85] values in the alloys (Table 6), significantly larger than in bcc Li. This illustrates that localized electrons also exist in these alloys, presumably within Si–Si bonds or around Si atoms. The ρ_{max}/ρ_0 and ρ_{max}/ρ_{0del} values in WGCD calculations (Table 6) confirm the existence of localized electrons; the values in alloy phases are very large, even larger than in CD Si. The average density becomes smaller due to volume expansion with increasing Li concentration, but localized electrons still exist, producing higher ρ_{max}/ρ_0 ratios. Finally, we observe the trend of maximum ELF decreasing with increasing Li concentration, which indicates that electron localization is indeed weaker with more Li. In the WGCD formalism, ρ_{total}/ρ_{0del} is used as the electron localization indicator due to the lack of orbital and ELF information. Thus, ρ_{max}/ρ_{0del} can be recognized as the equivalent counterpart in OFDFT of maximum ELF in KSDFT. However, at a quantitative level, we see inconsistent trends in these two values. ELF$_{max}$ generally decreases as the Li concentration increases and in CD Si it has its largest value. This makes sense since CD Si a purely covalent phase. ρ_{max}/ρ_{0del} values from OFDFT exhibit a different trend; it first increases and then decreases with more Li in the alloy, and the value in CD Si is actually the smallest except bcc Li. The inconsistency shows the limitation of using only densities as an electron localization indicator compared to ELF in KSDFT. Although, the WGCD formalism is qualitatively correct in separating localized and delocalized densities as discussed above, the specific method to determine levels of electron localization in different systems can be further improved. However, the results shown here are still quite promising and we believe a more sophisticated electron localization indicator and perhaps more elaborate decomposition scheme will further advance the accuracy and transferability of the WGCD KEDF model.

4.6. Li atom surface adsorption

As a final test, we calculate Li atom adsorption energies on the reconstructed Si(100) surface (Table 7) as first simple test of Li–Si mixing during lithiation of silicon. We employ a $p(2 \times 1)$ geometry where each two Si atoms on the surface form a buckled dimer (Fig. 1). We first put Li atoms in the troughs (site T) between dimer rows. OFDFT with both HC and WGCD KEDFs predict accurate energies compared to KSDFT, especially compared to PAW results through a fortuitous cancellation of errors in the BLPS and KEDF. We then push Li atoms deeper into the Si bulk. We choose two different sites beneath the first layer of the Si surface. KSDFT–PAW and KSDFT–BLPS give similar adsorption energies for these two sites, while OFDFT predicts more negative adsorption energies with both KEDFs (Table 7). As Li atoms beneath the surface distort the lattice, the total energies will increase and be higher compared to above-the-surface case (T site). The adsorption energy differences for the A and B sites with respect to the T site are also calculated (Table 7). We see a considerable discrepancy between KSDFT–PAW and KSDFT–BLPS calculations mainly due to different E_T values. BLPS energy differences are much smaller than PAW ones, meaning Li atoms may penetrate more easily into the Si bulk. The errors are entirely caused by the BLPS approximation and illustrate the importance of non-local effects. Both KEDFs within OFDFT predict positive energy differences. The WGCD model produces relatively smaller differences, while the HC KEDF gives an excellent result for the A site and an overestimate for the B site compared to KSDFT-BLPS results. This trend is consistent with the alloy formation energy results in Section 4.4. The WGCD KEDF gives too negative formation energies for small Li concentration cases; similarly, adsorption energies here are too negative, leading to

Table 7
Li atom adsorption energies (eV) on the Si(100) − 2 × 1 surface, calculated with KSDFT–PAW, KSDFT–BLPS, and OFDFT. For the A and B sites, the adsorption energy differences compared to the T site are also listed. $\lambda = 0.006$ and $\beta = 0.65$ are used in OFDFT–HC calculations; we employ $m = 0$, $a = 0.835$, and $b = 0.679$ in OFDFT–WGCD calculations.

	E_T	E_A	E_B	E_A–E_T	E_B–E_T
KSDFT–PAW	−2.231	−1.790	−1.801	+0.440	+0.430
KSDFT–BLPS	−1.793	−1.649	−1.662	+0.144	+0.131
OFDFT–WGCD	−2.345	−2.284	−2.287	+0.060	+0.058
OFDFT–HC	−2.432	−2.302	−2.184	+0.130	+0.248

Table 8
Average computational wall time (seconds) of KSDFT-PAW and KSDFT-BLPS calculations using 32 processors, and serial (one processor) OFDFT calculations with different KEDFs. $Li_{22}Si_5$ with 108 atoms in the unit cell is used for this set of comparisons.

	OFDFT−WT	OFDFT−CAT	OFDFTGCD	OFDFT−HC	KSDFT−BLPS	KSDFT−PAW
Wall time	94	124	290	4190	8434	5007

underestimated energy differences (potentially leading to too large a driving force for lithiation). In contrast, the HC alloy formation energy for LiSi is very close to the KSDFT−BLPS result, indicating its better accuracy for systems with lower Li concentrations. As a result, the HC surface adsorption energies are quite accurate, especially for the A site. Generally, the OFDFT results are qualitatively reasonable.

4.7. Computational efficiency

Finally, we compare computational cost for all methods. Because our ultimate interest is to study mechanical deformation mechanisms that will require relatively large sample sizes, numerical efficiency is also critical. In Table 8, we list the average computational wall time for the $Li_{22}Si_5$ electron density optimization (108-atom unit cell) by OFDFT with different KEDFs and also by KSDFT with BLPSs in ABINIT and PAW in VASP. Parallelization is used with 32 CPUs for all KSDFT calculations. We see the PAW method is generally more efficient than the BLPS calculations due to significantly reduced kinetic energy cutoffs that can be used in PAW calculations. All OFDFT wall time is reported with a single core calculation to ensure a reasonable length of time for the OFDFT calculation (our PROFESS code is also well parallelized). The WT KEDF features the smallest computational cost because it has a density-independent kernel in its non-local KEDF. The CAT nonlocal KEDF is a little bit (less than 2 times) slower due to its density-dependent kernel. The WGC wall time is not reported since it cannot converge this system; but in a well converged calculation, it is typically takes twice as long as the corresponding WT calculation. The WGCD model, which involves several iterations of WGC calculations (but each iteration is much faster to converge), is approximately three times slower than WT calculations. Finally, the HC KEDF, which suffers increased computational cost due to the required interpolation step and related convergence issues, is generally much slower than other KEDFs. Considering the different numbers of CPUs used in the KSDFT and OFDFT calculations, all OFDFT calculations are orders of magnitude faster than KSDFT. Moreover, all KEDFs scale quasi-linearly, including the HC KEDF, and therefore they will be increasingly more efficient than KSDFT calculations for larger systems. From all perspectives including accuracy, transferability, stability, convergence issues, and numerical efficiency, we consider the WGCD KEDF model to be particularly promising for large-scale simulation of Li−Si alloys.

5. Conclusions and outlook

Crystalline Li−Si alloys were investigated with OFDFT. We first used KSDFT calculations to verify the accuracy of BLPSs compared to PAW calculations. Optimized structures, bulk and elastic moduli, and also alloy formation energies generally show very small errors. We then employed BLPSs in OFDFT calculations to test various KEDF models. In particular, the HC and WGCD KEDFs recently proposed for covalent materials were closely examined. These two functionals predict quite reasonable cell lattice vectors, equilibrium volumes, and bulk moduli for all alloys. They represent a striking improvement over other modern KEDFs including the WT, WGC, and CAT functionals, which either fail to converge or produce unphysical results. Elastic constants computed with the WGCD KEDF are fairly reasonable especially for those alloys with higher Li concentrations. Alloy formation energies were also calculated using universal parameter sets in the HC and WGCD KEDFs. The HC KEDF exhibited unsatisfactory transferability among most alloys, although an accurate result was predicted for the low Li concentration alloy LiSi. By contrast, the WGCD functional favors formation of all alloys examined (as does KSDFT) and generates good formation energies for high Li concentration alloys, but greatly overestimates the formation energies of LiSi and $Li_{12}Si_7$. A similar problem is found when calculating Li adsorption energies on Si(100), which can be considered as an extremely-low-Li-concentration case. The WGCD KEDF underestimates the energy differences between T and A/B sites while the HC KEDF gives larger and more accurate results compared to KSDFT benchmarks. However, both functionals give qualitatively correct trends. Finally, we compared ground-state densities in each alloy. OFDFT densities are very close to KSDFT benchmarks, as judged by comparing maximum and minimum densities. A closer examination of density information shows that both electron localization and the fraction of electrons that are delocalized are reasonably captured within the WGCD formalism. However, the level of electron localization is not precisely determined; more sophisticated electron localization indicators or WGCD scale functions may help to improve the KEDF model.

Overall, the OFDFT results are quite encouraging with both of these nonlocal KEDFs designed for semiconductors. With the outstanding computational efficiency shown in Section 4.7, OFDFT has the ability to study much larger sample sizes than KSDFT is capable of studying. It can thus be used to study thicker Si nanowires or large surface structures while mimicking experimental conditions more realistically. Bulk properties, surface energies [61], and elastic softening are correctly reproduced by OFDFT, so it may be used to investigate mechanical deformation and failure during lithiation and delithiation. However, both KEDFs are not accurate enough to reproduce all alloy formation energies, which are closely related to the open circuit voltage [86,87]. One needs to be careful when calculating related quantities within the present OFDFT approximations, especially with the HC KEDF which predicts many positive alloy formation energies. However, the HC KEDF is quite accurate for low Li concentrations, which means that it can be used to study the beginning stages of lithiation. The reasonable HC Li-atom surface adsorption energies also indicate it would be promising to study Li atom diffusion in Si nanowires, as studied in Ref. [25]. By contrast, the WGCD KEDF overestimates alloy formation energies for low Li concentration alloys. The resulting larger driving force of initial Li−Si mixing might also overestimate the rate of mixing during the initial lithiation process. However, it is very accurate for high Li concentration alloys, starting from Li_7Si_3, aside from LiSi. Consequently, we would use the WGCD KEDF to study the latter part of lithiation process or delithiation processes, whenever the Li concentration is relatively high. Both KEDFs are clearly not perfect yet. They are not transferable enough for all phases, so unfortunately the entire lithiation and delithiation process cannot be modeled accurately with one universal KEDF yet. This is the main limitation of OFDFT at present, and care must be taken when choosing a suitable KEDF model to explore the problem of interest.

Future studies will work on KEDF models to improve especially alloy formation energies. Meanwhile, we will test OFDFT accuracy on amorphous Li–Si alloys, since anode materials are observed to undergo crystalline-to-amorphous transformations at room temperature. Molecular dynamics (MD) simulation using OFDFT forces will be necessary as well. A number of OFDFT MD studies [67,88–91] have been reported in literature and showed excellent results. Large-scale OFDFT MD simulations should be a useful tool to probe various interesting and critical questions in the silicon lithiation process, potentially offering new insights for anode material development.

Acknowledgments

References

[1] P. Limthongkul, Y.-I. Jang, N.J. Dudney, Y.-M. Chiang, Acta Mater. 51 (2003) 1103.
[2] M.N. Obrovac, L. Christensen, Electrochem. Solid-State Lett. 7 (2004) A93.
[3] J. Li, J.R. Dahn, J. Electrochem. Soc. 154 (2007) A156.
[4] Y. Wang, J.R. Dahn, J. Electrochem. Soc. 153 (2006) A2188.
[5] M. Winter, J.O. Besenhard, Electrochim. Acta 45 (1999) 31.
[6] R.A. Sharma, R.N. Seefurth, J. Electrochem. Soc. 123 (1976) 1763.
[7] B.A. Boukamp, G.C. Lesh, R.A. Huggins, J. Electrochem. Soc. 128 (1981) 725.
[8] L.Y. Beaulieu, T.D. Hatchard, A. Bonakdarpour, M.D. Fleischauer, J.R. Dahn, J. Electrochem. Soc. 150 (2003) A1457.
[9] S.-J. Lee, J.-K. Lee, S.-H. Chung, H.-Y. Lee, S.-M. Lee, H.-K. Baik, J. Power Sources 97 (2001) 191.
[10] W. Wang, P.N. Kumta, J. Power Sources 172 (2007) 650.
[11] C.J. Wen, R.A. Huggins, J. Solid State Chem. 37 (1981) 271.
[12] T.R. Anantharaman, Metallic Glasses: Production Properties and Applications, Trans Tech Publications, Aedermannsdorf, Switzerland, 1984.
[13] T.B. Massalski, in: T.B. Massalski (Ed.), Binary Alloys Phase Diagram, ASM International, Materials Park, OH, 1990, p. 2465.
[14] L.A. Stearns, J. Gryko, J. Diefenbacher, G.K. Ramachandran, P.F. McMillan, J. Solid State Chem. 173 (2003) 251.
[15] Y. Kubota, M.C.S. Escano, H. Nakanishi, H. Kasai, J. Appl. Phys. 102 (2007) 053704.
[16] Y. Kubota, M.C.S. Escano, H. Nakanishi, H. Kasai, J. Alloys Compd. 458 (2008) 151.
[17] H. van Leuken, G.A. de Wijs, W. van der Lugt, R.A. de Groot, Phys. Rev. B 53 (1996) 10599.
[18] V.B. Shenoy, P. Johari, Y. Qi, J. Power Sources 195 (2010) 6825.
[19] V.L. Chevrier, J.W. Zwanziger, J.R. Dahn, Can. J. Phys. 87 (2009) 625.
[20] H. Kim, C.-Y. Chou, J.G. Ekerdt, G.S. Hwang, J. Phys. Chem. C. 115 (2011) 2514.
[21] V.L. Chevrier, J.W. Zwanziger, J.R. Dahn, J. Alloys Compd. 496 (2010) 25.
[22] P. Johar, Y. Qi, V.B. Shenoy, Nano Lett. 11 (2011) 5494 and reference therein.
[23] V.L. Chevrier, J.R. Dahn, J. Electrochem. Soc. 156 (2009) A454.
[24] H. Kim, K.E. Kweon, C.Y. Chou, J.G. Ekerdt, G.S. Hwang, J. Phys. Chem. C 114 (2010) 17942.
[25] Q.F. Zhang, W.X. Zhang, W.H. Wan, Y. Cui, E.G. Wang, Nano Lett. 10 (2010) 3243.
[26] K. Zhao, G.A. Tritsaris, M. Pharr, W.L. Wang, O. Okeke, Z. Suo, J.J. Vlassak, E. Kaxiras, Nano Lett. 12 (2012) 4397.
[27] M.K.Y. Chan, C. Wolverton, J.P. Greeley, J. Am. Chem. Soc. 134 (2012) 14362.
[28] G.A. Tritsaris, K. Zhao, O.U. Okeke, E. Kaxiras, J. Phys. Chem. C 116 (2012) 22212.
[29] X.H. Liu, H. Zheng, L. Zhong, S. Huan, K. Karki, L.Q. Zhang, Y. Liu, A. Kushima, W.T. Liang, J.W. Wang, J.H. Cho, E. Epstein, S.A. Dayeh, S.T. Picraux, T. Zhu, J. Li, J.P. Sullivan, J. Cumings, C.S. Wang, S.X. Mao, Z.Z. Ye, S.L. Zhang, J.Y. Huang, Nano Lett. 11 (2011) 3312.
[30] K. Rhodes, N. Dudney, E. Lara-Curzio, C. Daniel, J. Electrochem. Soc. 157 (2010) A1354.
[31] X.H. Liu, J.Y. Huang, Energy Environ. Sci. 4 (2011) 3844.
[32] Y.A. Wang, E.A. Carter, in: S.D. Schwartz (Ed.), Theoretical Methods in Condensed Phase Chemistry, Kluwer, Dordrecht, 2000, p. 117.
[33] L. Hung, E.A. Carter, Chem. Phys. Lett. 475 (2009) 163.
[34] I. Shin, A. Ramasubramaniam, C. Huang, L. Hung, E.A. Carter, Philos. Mag. 89 (2009) 3195.
[35] Q. Peng, X. Zhang, L. Hung, E.A. Carter, G. Lu, Phys. Rev. B 78 (2008) 054118.
[36] L. Hung, E.A. Carter, J. Phys. Chem. C 115 (2011) 6269.
[37] G. Ho, E.A. Carter, J. Comput. Theor. Nanosci. 6 (2009) 1236.
[38] L. Hung, E.A. Carter, Modell. Simul. Mater. Sci. Eng. 19 (2011) 045002.
[39] I. Shin, E.A. Carter, Modell. Simul. Mater. Sci. Eng. 20 (2011) 015006.
[40] N. Choly, G. Lu, W. E, E. Kaxiras, Phys. Rev. B 71 (2005) 094101.
[41] X. Zhang, G. Lu, Phys. Rev. B 76 (2007) 245111.
[42] S.C. Watson, P.A. Madden, Phys. Chem. Commun. 1 (1998) 1.
[43] A. Aguado, J. López, J. Alonso, M. Stott, J. Chem. Phys. 111 (1999) 6026.
[44] G. Ho, C. Huang, E.A. Carter, Curr. Opin. Solid State Mater. Sci. 11 (2008) 57.
[45] E. Chacón, J.E. Alvarellos, P. Tarazona, Phys. Rev. B 32 (1985) 7868.
[46] P. García-González, J.E. Alvarellos, E. Chacón, Phys. Rev. B 53 (1996) 9509.
[47] P. García-González, J.E. Alvarellos, E. Chacón, Phys. Rev. B 57 (1998) 4857.
[48] D. García-Aldea, J.E. Alvarellos, Phys. Rev. A 76 (2007) 052504.
[49] L.W. Wang, M.P. Teter, Phys. Rev. B 45 (1992) 13196.
[50] F. Perrot, J. Phys. Condens. Matter 6 (1994) 431.
[51] E. Smargiassi, P.A. Madden, Phys. Rev. B 49 (1994) 5220.
[52] Y.A. Wang, N. Govind, E.A. Carter, Phys. Rev. B 58 (1998) 13465, 64 (2001) 129901–1(E).
[53] Y.A. Wang, N. Govind, E.A. Carter, Phys. Rev. B 60 (1999) 16350, 64 (2001) 089903(E).
[54] N.W. Ashcroft, N.D. Mermin, Solid State Physics, Holt Rinehart & Winston, Philadelphia, 1976.
[55] W.A. Harrison, Solid State Theory, Dover, New York, 1980.
[56] J. Lindhard, K. Dan, Vidensk. Selsk. Mat. Fys. Medd. 28 (1954) 8.
[57] R. Nesper, H.G. von Schnering, J. Curda, Chem. Berl. 119 (1986) 3576.
[58] H.G. von Schnering, R. Nesper, K.-F. Tebbe, J. Curda, Z. Metallkd. 71 (1980) 357.
[59] B. Key, R. Bhattacharyya, M. Morcrette, V. Seznéc, J.-M. Tarascon, C.P. Grey, J. Am. Chem. Soc. 131 (2009) 9239.
[60] C. Huang, E.A. Carter, Phys. Rev. B 81 (2010) 045206.
[61] J. Xia, E.A. Carter, Phys. Rev. B 86 (2012) 235109.
[62] J. Xia, C. Huang, I. Shin, E.A. Carter, J. Chem. Phys. 136 (2012) 084102.
[63] P. Hohenberg, W. Kohn, Phys. Rev. 136 (1964) B864.
[64] W. Kohn, L.J. Sham, Phys. Rev. 140 (1965) A1133.
[65] B. Zhou, Y.A. Wang, E.A. Carter, Phys. Rev. B 69 (2004) 125109.
[66] C. Huang, E.A. Carter, Phys. Chem. Chem. Phys. 10 (2008) 7109.
[67] M. Chen, L. Hung, C. Huang, J. Xia, E.A. Carter, Mol. Phys. 111 (2013) 3448.
[68] L.H. Thomas, Proc. Camb. Philos. Soc. 23 (1927) 542.
[69] E. Fermi, Rend. Accad. Naz. Lincei 6 (1927) 602.
[70] E. Fermi, Z. Phys. 48 (1928) 73.
[71] C.F. von Weizsäcker, Z. Phys. 96 (1935) 431.
[72] L. Hung, C. Huang, I. Shin, G. Ho, V.L. Ligneres, E.A. Carter, Comput. Phys. Commun. 181 (2010) 2208.
[73] J.P. Perdew, K. Burke, M. Ernzerhof, Phys. Rev. Lett. 77 (1996) 3865.
[74] P.E. Blöchl, Phys. Rev. B 50 (1994) 17953.
[75] G. Kresse, J. Hafner, Phys. Rev. B 47 (1993) 558.
[76] G. Kresse, J. Furthmuller, Comput. Mater. Sci. 6 (1996) 15.
[77] G. Kresse, J. Furthmuller, Phys. Rev. B 54 (1996) 11169.
[78] X. Gonze, J.-M. Beuken, R. Caracas, F. Detraux, M. Fuchs, G.-M. Rignanese, L. Sindic, M. Verstraete, G. Zerah, F. Jollet, M. Torrent, A. Roy, M. Mikami, Ph. Ghosez, J.-Y. Raty, D.C. Allan, Comput. Mater. Sci. 25 (2002) 478.
[79] F.D. Murnaghan, Proc. Natl. Acad. Sci. U. S. A. 30 (1944) 244.
[80] K. Momma, F. Izumi, J. Appl. Crystallogr. 41 (2008) 653.
[81] S.G. Louie, S. Froyen, M.L. Cohen, Phys. Rev. B 26 (1982) 1738.
[82] B. Zhou, V. Ligneres, E.A. Carter, J. Chem. Phys. 122 (2005) 044103.
[83] Z. Cui, F. Gao, Z. Cui, J. Qu, J. Power Sources 207 (2012) 150.
[84] B. Silvi, A. Savin, Nature 371 (1994) 683.
[85] A.D. Becke, K.E. Edgecombe, J. Chem. Phys. 92 (1990) 5397.
[86] M.K. Aydinol, A.F. Kohan, G. Ceder, K. Cho, J. Joannopoulos, Phys. Rev. B 56 (1997) 1354.
[87] M.K. Aydinol, G. Ceder, J. Electrochem. Soc. 144 (1997) 3832.
[88] M. Pearson, E. .Smargiassi, P.A. Madden, J. Phys. Condens. Matter 5 (1993) 3321.
[89] J.A. Anta, P.A. Madden, J. Phys. Condens. Matter 11 (1999) 6099.
[90] D.J. Gonzalez, L.E. Gonzalez, J.M. Lopez, M.J. Stott, J. Non-Cryst. Solids 312 (2002) 110.
[91] M. Foley, E. Smargiassi, P.A. Madden, J. Phys. Condens. Matter 6 (1994) 5231.